

# Dynamic Analysis of Radiation and Side-Mode Suppression in a Second-Order DFB Laser Using Time-Domain Large-Signal Traveling Wave Model

L. M. Zhang, S. F. Yu, M. C. Nowell, D. D. Marcenac, J. E. Carroll, and R. G. S. Plumb

**Abstract**—In this paper, we have developed a relatively simple algorithm to calculate the large-signal dynamic response of DFB lasers by solving the time-dependent coupled wave equations directly in the time domain. The spontaneous emission noise, longitudinal variations of carrier (hole burning) and photon densities as well as that of the refractive index are taken into consideration. To demonstrate the power of this straightforward algorithm, the model shows how the side-mode suppression ratio in devices with high  $\kappa L$  and a  $\lambda/4$  phase shift is significantly affected by the radiation in the second-order DFB laser. The time-dependent radiation pattern in grating-coupled surface-emitting lasers is also calculated for the first time.

## I. INTRODUCTION

SEMICONDUCTOR lasers with stable single-longitudinal-mode operation are essential components in long-haul, high bit-rate, optical transmission systems [1], [2]. The frequency selectivity of a Bragg grating makes lasers with distributed feedback (DFB) the favored device for single-mode operation. However, device designs have become more complex in order to overcome the two-moded degeneracy [3] of the lasing frequency when lasers, with uniform gratings and perfect antireflective (AR) coatings are used. For example the laser can have asymmetrically coated facets to encourage a single mode, but this occurs at the expense of an unpredictable lasing frequency caused by the uncertain phase of the facet reflection [4] relative to the grating. Introducing a  $\lambda/4$  phase shift [5], [6] in the grating structure is effective for achieving a single-mode operation. However, for such a phase-shifted laser, when the coupling coefficient is large ( $\kappa L > 3$ ), a significant number of photons concentrate around the phase shift region and cause severe hole burning. This hole burning is found to enhance the side mode [6]. To combat this hole burning and suppress the side mode, a variety of methods can be used such as modulating the grating pitch [7], [8], modulating the stripe width [9], and using multiple phase shifts ( $2 \times \lambda/8$ ) for example [10]. Many DFB lasers are made with second-order gratings because of the relative ease of construction with a longer pitch than for a first-order grating, although in general they have additional loss through the first-order radiation. In this paper, we show that this radiation can actually play an important role in determining the side-mode

suppression ratio (SMSR), particularly in high  $\kappa L$  devices. With certain designs of the grating structure, the first-order radiation can result in enhanced SMSR. The dynamics of side-mode suppression with such uniform lasers are studied briefly here.

Another important feature of the second-order DFB laser is that it diffracts the light vertically away from the laser junction through the radiation. Devices can be designed to use this effect and are known as grating-coupled surface-emitting (GSE) lasers [11]–[15]. They offer the potential of low beam divergence ( $< 0.012^\circ$  [17]) and high power output ( $> 1$  W [17]). GSE lasers can also be used in optical interconnects between wafers (chip to chip interconnection) [18], [19] or parallel optical signal processing [20] and coherent arrays [21], [22].

The theoretical analyses of GSE lasers [11]–[14], [23] are strong on the static properties but have difficulties with dynamics of the surface emission. However for applications using modulation, such as optical interconnection and optical signal processing, it is important to predict the dynamic behavior. The authors believe that this work offers the first self-consistent model that models the large-signal dynamic response of such devices.

The paper is organized as follows: in the next section, we will present a relatively simple self-consistent dynamic model based on a direct solution of the time-dependent coupled wave equations. The model takes account of the spontaneous emission, the longitudinal variations of carrier density, photon distribution, and the refractive index. In Section III, we will demonstrate the effects of the first-order radiation on the side mode in the second-order grating. The dynamic response of GSE lasers, including the time-dependent near- and far-field patterns, will be presented in Section IV. Conclusions are given in Section V.

## II. THEORY

There are several large-signal models that analyse the dynamic response through photonic [24] and traveling-wave [25] rate equations. However, these models in general have focused on Fabry–Perot lasers. The transmission line laser model [26] has become well established, and a power matrix model [27] based on the frequency domain have been developed particularly for DFB structures, the latter model providing an average response and eliminating the uncertainties of the phase

Manuscript received April 12, 1993; revised August 17, 1993. The work was supported by SERC.

The authors are with the Department of Engineering, Cambridge University, Trumpington Street, Cambridge, CB2 1PZ, England.  
IEEE Log Number 9400522.

of spontaneous emission. In this section we present a straightforward algorithm to calculate the dynamic response based on directly solving time-dependent coupled wave equations.

The electrical field in the waveguide can be written as

$$E(z, t) = [F(z, t)e^{-i\beta_0 z} + R(z, t)e^{i\beta_0 z}]e^{-i\omega_0 t} \quad (1)$$

where  $\omega_0$  is the reference frequency and  $\beta_0$  is the propagation constant at Bragg frequency.  $F$  and  $R$  represent the forward and reverse waves in the waveguide respectively. The fields  $F$  and  $R$  satisfy the time-dependent coupled wave equations [23], [27]

$$\begin{aligned} \frac{1}{c_g} \frac{\partial F(t, z)}{\partial t} + \frac{\partial F(t, z)}{\partial z} \\ = (g - i\delta - \alpha_s - h_1)F(t, z) \\ + i(\kappa + ih_1)R(t, z) + s_f \end{aligned} \quad (2)$$

$$\begin{aligned} \frac{1}{c_g} \frac{\partial R(t, z)}{\partial t} - \frac{\partial R(t, z)}{\partial z} \\ = (g - i\delta - \alpha_s - h_1)R(t, z) \\ + i(\kappa + ih_1)F(t, z) + s_r \end{aligned} \quad (3)$$

Here, the complex fields  $F$  and  $R$  include the amplitude and phase information. The spontaneous noise is driven by  $s_f$  and  $s_r$ , which couple into the forward and reverse fields,  $\kappa$  is the coupling coefficient between forward and reverse waves,  $c_g$  is the group velocity,  $h_1$  determines the radiation loss for the second order grating, and  $\alpha_s$  is the waveguide loss caused by free electron absorption and scattering. The field gain  $g$  is given by

$$g(z, t) = \frac{\Gamma g_N(N(z, t) - N_0)}{2(1 + \varepsilon P)} \quad (4)$$

where  $\Gamma$  is the confinement coefficient of the active layer,  $g_N$  is the differential gain,  $N_0$  is the carrier density at transparency,  $\varepsilon$  is the gain compression coefficient,  $N$  is the carrier density,  $P$  the photon density, and  $\delta$  is the deviation from the Bragg condition defined as

$$\delta = \frac{\omega_0}{c} n_{\text{eff}}(z, t) - \frac{\pi}{\Lambda}. \quad (5)$$

Here  $c$  is the speed of light at vacuum and  $\Lambda$  is the pitch of the grating.  $n_{\text{eff}}$  is the effective refractive index, which is related to the carrier density by

$$n_{\text{eff}}(z, t) = n_{\text{eff}0} - \Gamma \alpha_m g_N \Delta N(z, t). \quad (6)$$

The refractive index takes the value  $n_{\text{eff}0}$  at the carrier density  $N = N_0$ .  $\Delta N$  is the change of carrier density, and  $\alpha_m$  is the material linewidth enhancement factor.

The coupled equations (2) and (3) can be solved in the time domain by a first-order difference approximation to the partial differential:

$$\begin{aligned} \frac{\partial F(t, z)}{\partial t} &= \frac{F(t + \Delta t) - F(t, z)}{\Delta t} \quad \text{and} \\ \frac{\partial F(t, z)}{\partial z} &= \frac{F(t, z + \Delta z) - F(t, z)}{\Delta z} \end{aligned} \quad (7)$$

$$\begin{aligned} \frac{\partial R(t, z)}{\partial t} &= \frac{R(t + \Delta t) - R(t, z)}{\Delta t} \quad \text{and} \\ \frac{\partial R(t, z)}{\partial z} &= \frac{R(t, z) - R(t, z - \Delta z)}{\Delta z} \end{aligned} \quad (8)$$

If we choose the relation between time and spatial steps as  $\Delta z = c_g \Delta t$  and neglect the second derivative  $\partial^2 F(z, t)/\partial t \partial z$  and  $\partial^2 R(z, t)/\partial t \partial z$  (Appendix I), we can obtain the traveling wave formula as follows:

$$\begin{aligned} F(t + \Delta t, z + \Delta z) - F(t, z) \\ = \Delta z [(g - i\delta - \alpha_s - h_1)F(t, z) \\ + i(\kappa + ih_1)R(t, z) + s_f] \end{aligned} \quad (9)$$

$$\begin{aligned} R(t + \Delta t, z - \Delta z) - R(t, z) \\ = \Delta z [(g - i\delta - \alpha_s - h_1)R(t, z) \\ + i(\kappa + ih_1)F(t, z) + s_r] \end{aligned} \quad (10)$$

A more sophisticated model may allow the group velocity  $c_g$  to vary with change carrier density and then take this second-order variation onto the RHS of (9) and (10). However, here  $c_g$  is taken to be constant.

It is important to note that these 'traveling'-wave finite-difference equations do lead to the correct evanescent solutions at the center of the Bragg stop-band, as may be checked simply by putting  $g$ ,  $\delta$ ,  $\alpha_s$ ,  $h_1$ ,  $s_f$ , and  $s_r$  all to zero and solving the finite-difference equations (9) and (10).

The time-dependent carrier rate equation in the active layer is as usual

$$\frac{dN}{dt} = \frac{J}{ed} - BN^2 - CN^3 - \frac{g_N(N - N_0)}{1 + \varepsilon P} c_g P \quad (11)$$

where  $J$  is the current injection density,  $e$  is the electron charge,  $d$  is the thickness of the active layer,  $B$  and  $C$  are bimolecular and Auger recombination coefficients, respectively, and  $P$  is the photon density, which is given by the normalized power  $\{|F|^2 + |R|^2\}$ .

If we choose  $z = 0$  at the left-hand facet, the boundary condition for the forward and reverse waves at the facets can be written as

$$F(t, 0) = r_L R(t, 0) \quad \text{and} \quad R(t, L) = r_R F(t, L) \quad (12)$$

where  $r_L$  and  $r_R$  are the amplitudes of the facet reflections.

To take the spatial hole burning into consideration, the laser is divided into a number of equal small sections with length  $\Delta z = L/M$ , where  $L$  is the length of the laser and  $M$  is the number of sections. In each section, the material and structure parameters are assumed to be constant, but they are allowed to change from section to section. By knowing the field value at time  $t$  and location  $z$ , the field for forward (reverse) waves at the next time  $t + \Delta t$ , where  $\Delta t = \Delta z/c_g$ , can be determined at the position  $z + \Delta z(z - \Delta z)$  from (9) and (10). In each time step, the carrier density  $N$ , field gain  $g$ , and effective index will change according to (5), (6) and (11). A  $90^\circ$  phase shift is inserted at the center of the structure to simulate the  $\lambda/4$  phase shift. Since the length of the  $\lambda/4$  phase shift is much smaller than the length of each section, the time delay of this phase shift can be neglected. The phase of the facet reflection is treated in the similar way as the central  $\lambda/4$  phase shift. The spontaneous noise is generated from a Gaussian distributed random number generator [28] that satisfies the correlation

$$\begin{aligned} \langle s(z, t) s^*(z', t) \rangle &= \beta K R_{sp} \delta(t - t') \delta(z - z') / c_g \quad \text{and} \\ \langle s(z, t) s(z', t) \rangle &= 0 \end{aligned} \quad (13)$$

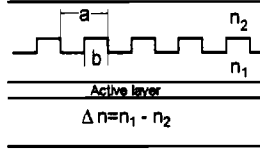


Fig. 1. Schematic structure of the rectangular grating.

here  $R_{sp} = BN^2/L$  is the bimolecular recombination per unit length contributed to spontaneous emission,  $\beta$  is the spontaneous coupling factor, and  $K$  is the transverse Petermann factor. It has been proved by Petermann [29] that the spontaneous emission fields coupled to the forward and reverse waves have equal amplitudes, e.g.,  $s(z, t) = s_f(z, t) = s_r(z, t)$ .

The equations (9), (10), (5), (6), and (11) can be solved by computer. There were no numerical problems apparent for our simulation. The effect of the second-order terms  $\partial^2 F(z, t)/\partial t \partial z$  and  $\partial^2 R(z, t)/\partial t \partial z$  is reduced approximately as  $M^{-2}$  as we increase the section number  $M$ . For  $M > 20$ , the effect of these terms can be negligible, with steady convergence of the results as the number of sections is increased.

It is also worth contrasting this time domain model with the power matrix model [27]. The power matrix model saves some time by calculating average power levels, while time-domain models are stochastic when driven by random spontaneous emission. They have to be run for long enough, or have multiple runs, so that sensible averages can be made. However the power matrix model requires the computer to keep track of all the significant modes, especially if one wishes to calculate side-mode suppression ratios. It is here that time domain models can make up computational time and give computational simplicity by automatically calculating the superposition of all the modes together separating the modes only after Fourier analysis. Uniform and  $\lambda/4$  phase-shifted DFB structures have been simulated on both models with very good agreement between them.

### III. EFFECT OF RADIATION ON SIDE-MODE SUPPRESSION

The radiation coefficient  $h_1$  (loss) can be solved from the static coupled wave equations through the Green's function method [23]. Although the radiation coefficient is always a positive number, the sign of  $\kappa$  can be either positive or negative, depending on the grating geometry. For the rectangular grating shown in Fig. 1, the  $\kappa$  is negative (positive) if  $b < a/2$  ( $b > a/2$ ), and the radiation is coupled vertically from the laser junction. The ratio  $h_1/|\kappa|$  of the first- and second-order coefficients is found to be of the magnitude of 0.1 [23]. Although the actual value strongly depends on the detail of the grating, 0.1 is believed to be a reasonable estimate and will be adopted in the rest of this paper.

In this section, we will concentrate on the commonly used 'single-mode'  $\lambda/4$  phase shift DFB laser. The phase shift is placed at the center of the grating. The laser is assumed to have perfect AR coating with facet reflections  $r_L = r_R = 0$ . Other material and structure parameters used in our modeling

TABLE I  
PARAMETERS USED IN THE MODEL

Bimolecular carrier recombination coefficient (B)	$1 \cdot 10^{10} \text{ cm}^3 \text{ s}^{-1}$
Auger carrier recombination coefficient (C)	$3 \cdot 10^{29} \text{ cm}^6 \text{ s}^{-1}$
Differential gain ( $g_N$ )	$3 \cdot 10^{16} \text{ cm}^2$
Transparency carrier density ( $N_0$ )	$1.5 \cdot 10^{18} \text{ cm}^{-3}$
Linewidth enhancement factor ( $\alpha_m$ )	4.86
Absorption and scattering loss in wave guide ( $\alpha_s$ )	$40 \text{ cm}^{-1}$
Effective phase refractive index ( $n_{eff0}$ )	3.283
Effective group refractive index ( $n_g$ )	3.70
Wave guide confinement factor ( $\Gamma$ )	0.35
Length of the laser cavity ( $L$ )	$400 \mu\text{m}$
Thickness of the active layer ( $d$ )	$0.18 \mu\text{m}$
Spontaneous coupling factor ( $\beta$ )	$10^{-4}$
Petermann factor ( $K$ )	1
Approximate emission wavelength ( $\lambda_0$ )	$1.55 \mu\text{m}$
Nonlinear gain suppression coefficient ( $\epsilon$ )	$3 \cdot 10^{-17} \text{ cm}^3$

are listed in Table I. To optimize between the calculation accuracy and computation time, we have divided the laser into 40 sections, as further increase in section number only gives a little improvement on the accuracy.

A DFB laser device with high coupling coefficient length product  $\kappa L = 3.2$  is chosen in order to emphasize the side mode effects. The laser was initially biased at close to the threshold  $J_0 = 2200 \text{ A/cm}^2$ , which was calculated from static light-current characteristics. Then the laser was switched to a high current level  $J_a = 5500 \text{ A/cm}^2$ , characterized by a step function

$$J(t) = J_0 + (J_a - J_0)h(t) \quad (14)$$

where  $h(t)$  is the step function given by

$$h(t) = \begin{cases} 0 & t < 0 \\ 1 & t > 0 \end{cases} \quad (15)$$

To demonstrate the effects of radiation on the side-mode suppression ratio, we compare a laser using a first-order grating (no radiation) with one using a second-order grating. Both structures are assumed to have the same  $\kappa L$ . For a direct comparison, we set the waveguide loss for the first-order grating  $\alpha_s^{(1)} = h_1 + \alpha_s^{(2)}$ , where  $\alpha_s^{(2)}$  is the waveguide loss for the second-order grating. An approximation of  $\sqrt{(\kappa^2 + h_1^2)} \approx \kappa$  is used since  $h_1/|\kappa|$  is relatively small. Figure 2 shows the transient response to the step function  $h(t)$  for a first-order DFB laser. When the laser first switches on, there is a pulse with no mode beating, but after nearly 1 ns the output power starts to oscillate in small amplitude as a consequence of beating between two modes. This is confirmed by transforming the time-dependent field using a fast Fourier transform with a Hamming window. Figure 3(a) shows the spectrum of the first pulse in which good single-mode operation (oscillating at the center of the stop band) is demonstrated. The broadening of the spectrum indicates that the pulse is chirped. Figure 3(b) shows the spectrum [with the same scale as Fig. 3(a)] of the oscillating signal from 2 ns to 3 ns, in which the side mode can be clearly seen. The occurrence of this side mode results in a poor SMSR. The side mode is found to be further enhanced as the injection current increases. Severe hole burning in high  $\kappa L$  devices is considered to be the cause of this poor SMSR [6].

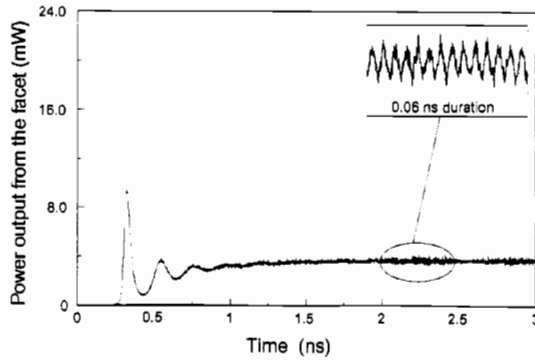
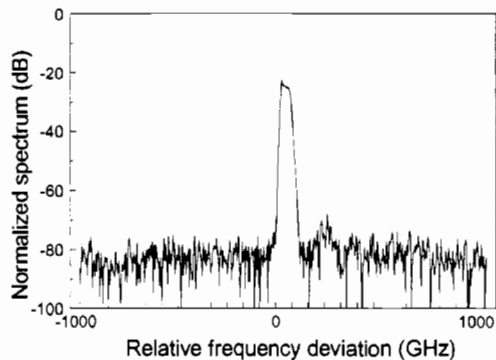
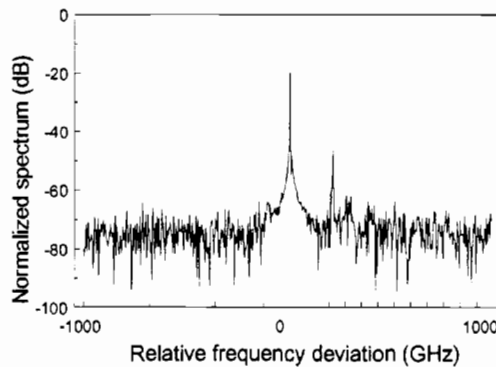


Fig. 2. Transient response (current from  $J = J_0$  to  $J = J_a$ ) of power output from first-order grating DFB laser. The laser has coupling coefficient  $\kappa = 80 \text{ cm}^{-1}$  and no first-order radiation. The small window at top left shows the beating of two modes.



(a)



(b)

Fig. 3. Fourier transform spectra of time domain signal given in Fig. 2. Spectrum of (a) 250-ps window covering the first pulse, (b) a window covering the last 1-ns.

In contrast, we also calculate a second-order DFB laser under the same driving condition. Figure 4 shows the transient response with  $\kappa = 80 \text{ cm}^{-1}$ . The transient signal displays good single-mode operation from the start, without the beating that is indicative of a second mode of oscillation. The beneficial effects of radiation loss in gaining single-mode operation have been noted for uniform lasers [31], but then the single mode oscillation occurs at the appropriate edge of the stop band

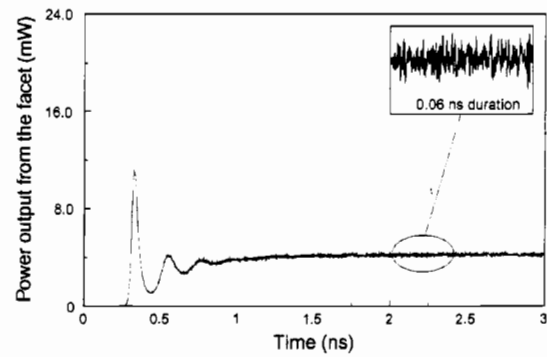


Fig. 4. Similar to Fig. 2 but calculated for second-order grating DFB laser with  $\kappa = +80 \text{ cm}^{-1}$  and first-order radiation loss  $h_1 = 5 \text{ cm}^{-1}$

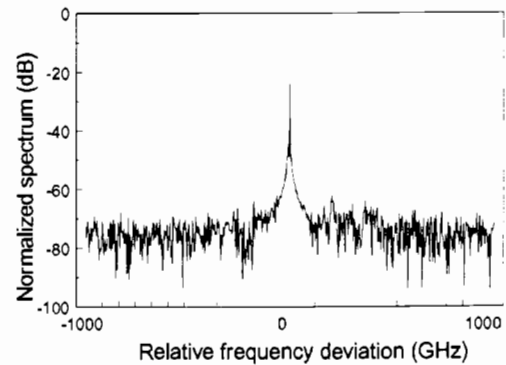


Fig. 5. Fourier transform spectrum of time domain signal (last 1 ns) given in Fig. 4.

rather than as here at the center. The Fourier spectrum of Fig. 4 is plotted in Fig. 5. However, with  $\kappa = -80 \text{ cm}^{-1}$ , a completely different transient response can also be obtained, as shown in Fig. 6. The laser initially oscillated in a single mode in the center of the stop band (without beating), but after 0.5 ns it became two moded (with strong beating) exhibiting the similar effect to Fig. 3 but even more strongly. Figure 7 gives the Fourier transform of the time-domain signal for the interval from 2 ns to 3 ns after the current drive is applied. The above simulation suggests that the geometry of the grating can be important in the design of a second-order DFB laser. For a rectangular grating illustrated in Fig. 1, if one designs the second-order grating structure such that  $b > a/2$ , then  $\kappa > 0$  and a stable single-mode operation with a significantly improved SMSR should be achieved, according to the simulation.

For a DFB structure with a  $\lambda/4$  phase shift at the center and nonuniform distribution of carrier and photon densities, it is difficult to give an analytical analysis of the above phenomenon. However, the physics can be understood by examining numerically the interference between the forward (F) and reverse (R) waves in the grating structure [31]. With AR-coated facets, the interference between the F and R waves at the ends of the cavity is small. Strong interference is expected at the center where both F and R have their maxima. At the center, the power in the main mode at the

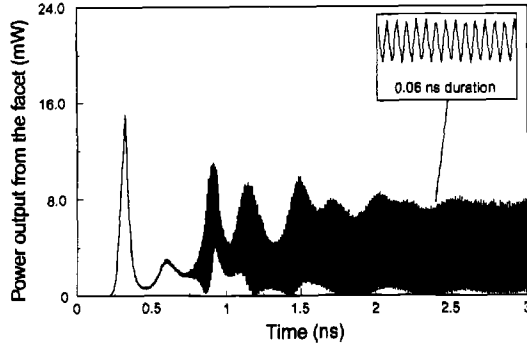
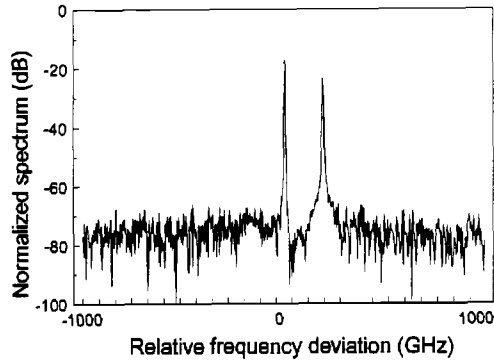

 Fig. 6. Same as Fig. 4 but  $\kappa = -80 \text{ cm}^{-1}$ .


Fig. 7. Fourier transform spectrum of time domain signal (last 1 ns) given in Fig. 4.

center of the stop band  $\omega = \omega_m$  is given by the sum of the squares,  $|\mathbf{F}(\omega, L/2)|^2 + |\mathbf{R}(\omega, L/2)|^2$ , where  $\mathbf{F}(\omega, L/2)$  and  $\mathbf{R}(\omega, L/2)$  are Fourier transforms of the time domain fields,  $F(t, L/2)$  and  $R(t, L/2)$ , respectively. However, in contrast the first-order radiation power is determined by the interference between the two fields, being proportional to the square of the sum:  $|\mathbf{F}(\omega, L/2) + \mathbf{R}(\omega, L/2)|^2$  (see next section). For  $\kappa > 0$ , we found for the main mode:

$$\begin{aligned} & |\mathbf{F}(\omega_m, L/2)|^2 + |\mathbf{R}(\omega_m, L/2)|^2 \\ & > |\mathbf{F}(\omega_m, L/2) + \mathbf{R}(\omega_m, L/2)|^2 \end{aligned} \quad (16)$$

while for the side mode at frequency  $\omega_s$

$$\begin{aligned} & |\mathbf{F}(\omega_s, L/2)|^2 + |\mathbf{R}(\omega_s, L/2)|^2 \\ & < |\mathbf{F}(\omega_s, L/2) + \mathbf{R}(\omega_s, L/2)|^2. \end{aligned} \quad (17)$$

Equation (16) indicates destructive interference radiation in the main mode, with equation (17) indicating constructive interference in the side mode [31]. Comparing the spectrum of first-order grating shown in Fig. 3(b), the second-order grating results in lower radiation loss in the main mode and higher radiation loss in side mode. This increases the gain margin between the main and side mode, which results in improvement of the SMSR. If  $\kappa < 0$ , (16) and (17) have their inequalities changed, so giving the opposite results. The side mode now has less radiation loss than the main mode. This decreases the gain margin between main and side mode and therefore results in a poor SMSR.

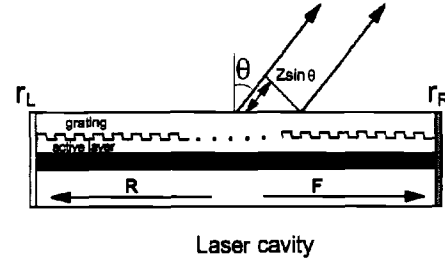


Fig. 8. Schematic structure of the second-order grating DFB lasers.

#### IV. DYNAMIC BEHAVIOR OF GSE LASERS

The GSE structure used in this paper is schematically shown in Fig. 8. The time-dependent near-field radiated pattern from the surface can be calculated from the amplitudes of forward and reverse waves [32]

$$E_{\text{near}}(z, t) \sim F(z, t) + R(z, t) \quad (18)$$

the angle distribution of the longitudinal far-field amplitude can be calculated from

$$\begin{aligned} E_{\text{far}}(\theta, t) \sim \cos(\theta) \int_{-\infty}^{\infty} & \left[ F\left(z, t - \frac{z \sin(\theta)}{c}\right) \right. \\ & \left. + R\left(z, t - \frac{z \sin(\theta)}{c}\right) \right] \\ & \cdot e^{-i[\omega_0(t - (z \sin(\theta)/c))]} dz \end{aligned} \quad (19)$$

where  $\theta$  (shown in Fig. 8) is the angle deviated from the surface normal in the longitudinal direction. The longitudinal fields  $F(z, t)$  and  $R(z, t)$  used in (19) can be obtained using linear interpolation from the sampled field  $[F(z_m, t_m)$  and  $R(z_m, t_m)]$  calculated from the model.

As an example, we have simulated a GSE uniform DFB laser with  $\kappa L = 2(\kappa = 50)$ . Two facets are assumed to have perfect AR coating ( $r_L = r_R = 0$ ). The time-dependent near-field intensity pattern  $|F(z, t) + R(z, t)|^2$  is shown in Fig. 9, while the angle distribution of the far field is shown in Fig. 10. The near-field pattern indicates a null at the center of the laser cavity. This phenomenon can be explained by the destructive interference between the forward and reverse waves [31]. The far-field pattern shows a double-lobe, which agrees well with a calculation based on the transfer matrix method [32]. Near and far fields can both be affected by facet reflection. In Figs. 11 and 12, we show the turn-on transient of near- and far-field patterns with one facet AR coating ( $r_L = 0$ ) and the other facet with HR coating ( $r_R = 0.8 \angle 180^\circ$ ). The near field has an asymmetric intensity distribution with high field intensity on the AR coating side while the far-field pattern displays single lobe radiation at the center of the cavity.

#### V. CONCLUSIONS

Based on well-known time-dependent coupled wave equations, we have developed a straightforward algorithm to model the large-signal dynamic behavior of DFB lasers. This self-consistent model takes account of the important nonlinear longitudinal hole burning and the refractive index change

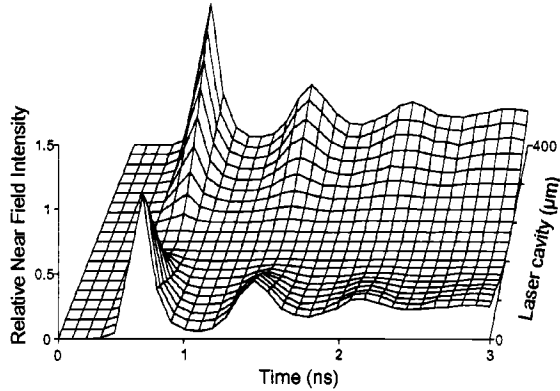


Fig. 9. The near-field pattern of GSE laser with AR coating on both facets.

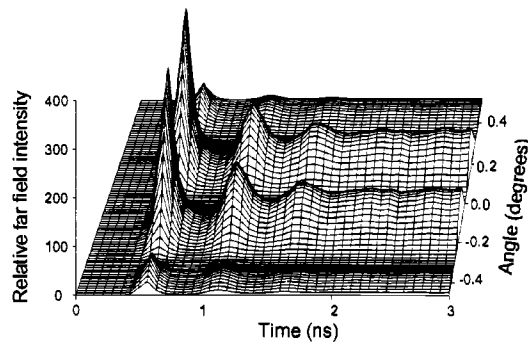
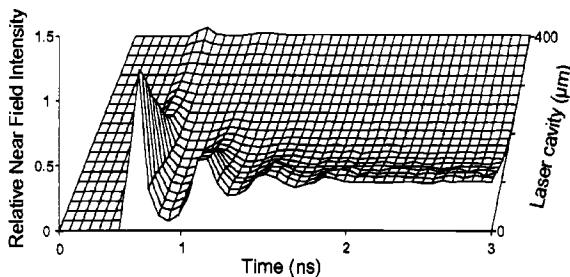


Fig. 10. The far-field angle distribution of GSE laser with AR coating on both facets.

Fig. 11. The near-field pattern of GSE laser with AR-HR coating. HR at  $L = 0$  and AR at  $L = 400 \mu\text{m}$ .

induced by carrier density. The random Gaussian distributed noise is considered to be the 'driving force' to the laser, and the complex fields  $F(z, t)$  and  $R(z, t)$  are calculated in the time domain. The possible multimode operation of the laser is automatically considered, while the frequency (modal) characteristics are calculated through Fourier transforms over appropriate windows of time. Because the model is directly connected with the coupled wave equations, the second-order effects and gain coupled gratings can be taken into consideration in a straightforward way.

The simulation program is written in FORTRAN 77 run on an IBM PC/486 with 66-MHz clock rate. It takes approx-

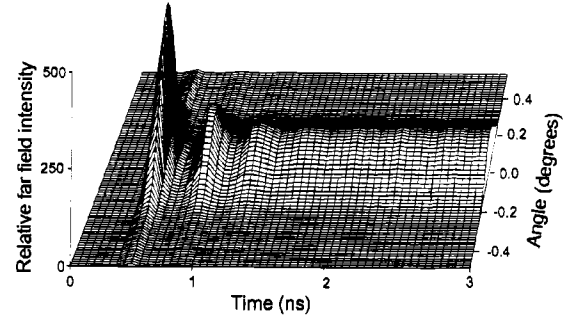


Fig. 12. The far-field angle distribution of GSE laser with AR-HR coating.

imately 40 seconds to simulate 2 ns dynamic response for a laser with 40 sections. The short computational time has helped enormously in interactive laser design, for example in new low-chirp lasers [33].

We have demonstrated the importance of the first-order radiation in second-order  $\lambda/4$  phase shift DFB lasers as an application of the model. For a first-order grating with high  $\kappa L$ , the side mode will be enhanced as the injection current increases. By taking account of the first-order radiation in a second-order grating, the SMSR can be either enhanced or reduced depending on the geometry of the grating. For the rectangular grating with duty cycle greater than 50% ( $b > a/2$ ) in Fig. 8), a significant increase of SMSR is possible. The simulation shows that more than 25-dB increase of SMSR can be obtained for a  $\kappa L = 3.2\lambda/4$  DFB laser at modest injection levels.

The dynamic response of a second-order GSE DFB laser is also calculated in this paper for the first time. The turn-on transient of the near- and far-field patterns as a function of time is simulated. Single-lobe radiation with asymmetric near-field distribution for AR-HR and double lobes with symmetric near field for AR-AR GSE DFB are demonstrated. Although we have only simulated the dynamic response of a relatively simple GSE structure, more complex devices such as coherent GSE arrays with separate DBR and gain sections can also be analyzed using this model and will form the subject of a future study.

#### APPENDIX

The LHS of (9) can be expanded as follows

$$\begin{aligned}
 & F(t + \Delta t, z + \Delta z) - F(t, z) \\
 &= F(t + \Delta t, z + \Delta z) - F(t, z + \Delta z) \\
 &\quad + F(t, z + \Delta z) - F(t, z) \\
 &= \frac{\partial F}{\partial t} \Big|_{z+\Delta z} \Delta t + \frac{\partial F}{\partial z} \Big|_t \Delta z = \frac{\partial F}{\partial t} \Big|_{z+\Delta z} \\
 &\quad \cdot \Delta t - \frac{\partial F}{\partial t} \Big|_z \Delta t + \frac{\partial F}{\partial t} \Big|_z \Delta t + \frac{\partial F}{\partial z} \Big|_t \Delta z \\
 &= \frac{\partial F}{\partial t} \Big|_z \Delta t + \frac{\partial F}{\partial z} \Big|_t \Delta z = \frac{\partial^2 F}{\partial t \partial z} \Delta z \Delta t \quad (A1)
 \end{aligned}$$

if we neglect the second-order term, take  $\Delta z = \Delta t^* c_g$ , and use the coupled wave equation. Equation (10) can be derived in the similar way.

#### ACKNOWLEDGMENT

The authors thank Dr. J. E. A. Whiteaway of BNR(Europe) for his helpful discussions.

#### REFERENCES

- [1] K. Nosu and K. Iwashita, "A consideration of factors affecting future coherent lightwave communication systems," *J. Lightwave Technol.*, vol. 6, pp. 686–694, 1988.
- [2] J. D. Barry, "Design and system requirements imposed by the selection of GaAs/GaAlAs single mode laser diodes for free-space optical communications," *IEEE J. Quantum Electron.*, vol. QE-20, pp. 478–491, 1984.
- [3] H. Kogelnik and C. V. Shank, "Coupled-wave theory of distributed feedback lasers," *J. Appl. Phys.*, vol. 43, pp. 2327–2335, 1972.
- [4] J. Buus, "Mode selectivity in DFB lasers with cleaved facets," *Electron. Lett.*, vol. 21, pp. 179–180, 1985.
- [5] H. A. Haus and C. V. Shank, "Antisymmetric taper of distributed feedback laser," *IEEE J. Quantum Electron.*, vol. QE-12, pp. 532–539, 1976.
- [6] J. E. A. Whiteaway, G. H. B. Thompson, A. J. Collar, and C. J. Armistead, "The design and assessment of  $\lambda/4$  phase-shift DFB laser structure," *IEEE J. Quantum Electron.*, vol. 25, pp. 1761–1779, 1989.
- [7] Y. Nakano and K. Tada, "Analysis, design, and fabrication of GaAlAs/GaAs DFB with modulated stripe width structure for complete single longitudinal mode oscillation," *IEEE J. Quantum Electron.*, vol. 24, pp. 2017–2033, 1988.
- [8] J. E. A. Whiteaway, B. Garrett, G. H. B. Thompson, A. J. Collar, C. J. Armistead, and M. J. Fice, "The static and dynamic characteristics of single and multiple phase-shifted DFB laser structures," *IEEE J. Quantum Electron.*, vol. 28, pp. 1277–1293, 1992.
- [9] P. Zhou and G. S. Lee, "Chirped grating  $\lambda/4$  shifted DFB laser with uniform longitudinal field distribution," *Electron. Lett.*, vol. 26, pp. 1660–1661, 1990.
- [10] H. Hillmer, K. Magari, and Y. Suzuki, "Chirped grating for DFB laser diode using bent waveguides," *IEEE Photonics Technol. Lett.*, vol. 5, pp. 10–12, 1993.
- [11] S. M. Macomber, "Nonlinear analysis of surface-emitting distributed feedback lasers," *IEEE J. Quantum Electron.*, vol. 26, pp. 2065–2074, 1990.
- [12] A. Hardy, D. F. Welch, and W. Streifer, "Analysis of second order gratings," *IEEE J. Quantum Electron.*, vol. 25, pp. 1989–2105, 1989.
- [13] R. Amantea, N. W. Carlson, S. L. Palfrey, G. A. Evans, J. M. Hammer, and M. Lurie, "Network analysis of the modes of two-dimensional grating-surface-emitting diode laser array," *IEEE J. Quantum Electron.*, vol. 26, pp. 1023–1038, 1990.
- [14] S. H. Macomber, J. S. Mott, R. J. Noll, G. M. Gallatin, E. J. Gratix, S. L. O'Dwyer, and S. A. Lambert, "Surface-emitting distributed feedback semiconductor laser," *Appl. Phys. Lett.*, vol. 51, pp. 472–474, 1987.
- [15] K. Mitsunaga, M. Kameya, K. Kojima, S. Noda, K. Kyuma, K. Hamanaka, and T. Nakayama, "CW surface-emitting grating-coupled GaAs/AlGaAs distributed laser with very narrow beam divergence," *Appl. Phys. Lett.*, vol. 50, pp. 1788–1790, 1987.
- [16] D. F. Welch, R. Parke, A. Hardy, W. Streifer, and D. R. Scifres, "High power grating coupled surface emitters," *Electron. Lett.*, vol. 25, pp. 819–820, 1989.
- [17] N. W. Carlson, G. A. Evans, J. M. Hammer, M. Lurie, L. A. Carr, F. Z. Hawrylo, E. A. James, C. J. Kaiser, J. B. Kirk, W. F. Reichert, D. A. Truxal, J. R. Shealy, S. R. Chinn, and P. S. Zory, "High power seven-element grating surface emitting diode laser array with 0.012 far-field angle," *Appl. Phys. Lett.*, vol. 52, pp. 939–941, 1988.
- [18] J. A. Neff, "Major initiatives for optical computing," *Opt. Eng.*, vol. 26, no. 2, pp. 2–9, 1987.
- [19] See papers inside the "Special issue on optical interconnects," *Opt. and Quantum Electron.*, vol. 24, April 1992.
- [20] A. Hartmann and S. Redfield, "Design sketches for optical crossbar switches intended for large scale parallel processing application," *Opt. Eng.*, vol. 28, no. 4, pp. 315, 1988.
- [21] N. W. Carlson, G. A. Evans, J. M. Hammer, M. Lurie, S. L. Palfrey, and A. Dholakia, "Phase-locked operation of a grating-surface-emitting diode laser array," *Appl. Phys. Lett.*, vol. 50, pp. 1301–1303, 1987.
- [22] G. A. Evans, N. W. Carlson, J. M. Hammer, M. Lurie, J. K. Butter, S. L. Palfrey, R. Amantea, L. A. Carr, F. Z. Hawrylo, E. A. James, C. J. Kaiser, J. B. Kirk, W. F. Reichert, S. R. Chinn, J. R. Shealy, and P. S. Zory, "Coherent monolithic two-dimensional ( $10 \times 10$ ) laser arrays using grating surface emission," *Appl. Phys. Lett.*, vol. 53, pp. 2123–2125, 1988.
- [23] R. F. Kazarinov and C. H. Henry, "Second-order distributed feedback lasers with mode selection provided by first order radiation losses," *IEEE J. Quantum Electron.*, vol. QE-21, pp. 144–150, 1985.
- [24] D. Marcuse and T. P. Lee, "On approximate analytical solution of rate equation for studying transient spectra of injection lasers," *IEEE J. Quantum Electron.*, vol. QE-19, pp. 1397–1406, 1983.
- [25] Y. L. Wong and J. E. Carroll, "A travelling-wave rate equation analysis for semiconductor lasers," *Solid-State Electron.*, vol. 30, pp. 13–19, 1987.
- [26] A. J. Lowery, "New dynamic model for multimode chirp DFB semiconductor lasers," *IEE Proc.*, Pt. J, vol. 137, pp. 293–300, 1990.
- [27] L. M. Zhang and J. E. Carroll, "Large signal dynamic model of the DFB laser," *IEEE J. Quantum Electron.*, vol. 28, pp. 604–611, 1992.
- [28] D. D. Marcenac and J. E. Carroll, "A new quantum mechanical model for realistic Fabry–Perot lasers," *Proc. Inst. Elec. Eng.*, Pt. J, vol. 140, pp. 157–171, 1993.
- [29] K. Petermann, "Calculated spontaneous emission factor for double heterostructure injection lasers with gain induced mode guiding," *IEEE J. Quantum Electron.*, vol. QE-15, pp. 556–570, 1979.
- [30] G. Morthier, P. Vankwikelberge, K. David, and R. Baets, "Improved performance of AR-coated DFB lasers by the introduction of gain coupling," *IEEE Photon. Technol. Lett.*, vol. 2, pp. 170–172, 1990.
- [31] C. H. Henry, R. F. Kazarinov, R. A. Logan, and R. Yen, "Observation of destructive interference in the radiation loss of second-order distributed feedback lasers," *IEEE J. Quantum Electron.*, vol. QE-21, pp. 151–154, 1985.
- [32] S. F. Yu, L. M. Zhang, R. G. S. Plumb, and J. E. Carroll, "Effect of external reflectors on radiation profile of grating coupled surface emitting lasers," *Proc. Inst. Elec. Eng.*, Pt. J, vol. 140, pp. 30–38, 1993.
- [33] M. C. Nowell, L. M. Zhang, and J. E. Carroll, "Low chirp push-pull modulation of three section DFB lasers," presented at Semiconductor and Integrated Optoelectronics, Cardiff 93.

**L. M. Zhang**, photograph and biography not available at the time of publication.

**S. F. Yu**, photograph and biography not available at the time of publication.

**M. C. Nowell**, photograph and biography not available at the time of publication.

**D. D. Marcenac**, photograph and biography not available at the time of publication.

**J. E. Carroll**, photograph and biography not available at the time of publication.

**R. G. S. Plumb**, photograph and biography not available at the time of publication.